


Semiclassical approach for solving the time-dependent Schrödinger equation in spatially inhomogeneous electromagnetic pulses

Jianxiong Li  and Uwe Thumm 

Department of Physics, Kansas State University, Manhattan, Kansas 66506, USA



(Received 15 November 2019; published 9 January 2020)

To solve the time-dependent Schrödinger equation in spatially inhomogeneous pulses of electromagnetic radiation, we propose an iterative semiclassical complex trajectory approach. In numerical applications, we validate this method against *ab initio* numerical solutions by scrutinizing (a) electronic states in combined Coulomb and spatially homogeneous laser fields and (b) streaked photoemission from hydrogen atoms and plasmonic gold nanospheres. In comparison with streaked photoemission calculations performed in strong-field approximation, we demonstrate the improved reconstruction of the spatially inhomogeneous induced plasmonic infrared field near a nanoparticle surface from streaked photoemission spectra.

DOI: [10.1103/PhysRevA.101.013411](https://doi.org/10.1103/PhysRevA.101.013411)

I. INTRODUCTION

The exposure of gaseous atomic, mesoscopic, and solid targets to incident pulses of electromagnetic radiation of sufficiently high photon energy or intensity leads to the emission of photoelectrons [1]. For more than a century, photoelectron spectroscopy has very successfully exploited this phenomenon and has long become established as one of the most prolific techniques for unraveling the *static* electronic structure of matter by examining the kinetic energy or momentum distribution of emitted photoelectrons. More recently, starting in the 21st century, advances in ultrafast laser technology started to extend photoemission spectroscopy into the time domain [2–4]. Importantly, the development of attosecond streaking [5,6] and interferometric [7–9] photoelectron spectroscopy enabled the observation of electron dynamics at the natural timescale of the electron motion in matter (attoseconds, $1 \text{ as} = 10^{-18} \text{ s}$). This was demonstrated in proof-of-principle experiments for gaseous atomic [10–16] and molecular [17–19] targets. Attosecond time-resolved photoemission spectroscopy is currently being extended to complex targets [6,20], such as nanostructures and nanoparticles [21–28], and solid surfaces [9,29–36], making it possible to examine, for example, the dynamics of photoemission from a surface on an absolute timescale [37] and suggesting, for example, the time-resolved observation of the collective motion of electrons (plasmons) in condensed-matter systems [38–40].

In combination with advances in nanotechnology, allowing the production of plasmonic nanostructures with increasing efficiency at the nm length scale, attosecond photoemission spectroscopy has started to progress toward the spatiotemporal imaging of electron dynamics in complex targets, approaching the atomic length and timescales (nm and attoseconds) [20,21,25–28,31,41,42]. Photoemission spectroscopy therefore holds promise to become a powerful tool for examining nm-attosecond scale processes that are operative in plasmonically enhanced photocatalysis [43], light harvesting [44], surface-enhanced Raman spectroscopy [45], biomedical and chemical sensing [46], tumor detection and treatment [47],

and ultrafast electro-optical switching [48]. The concurrent development and provision of large-scale light sources, capable of producing intense ultrashort pulses in the extreme ultraviolet (XUV) to x-ray spectral range at several leading laboratories in Europe, the United States, and Japan [49,50], promises to further boost the value of spatiotemporally resolved electron spectroscopy as a tool for imaging electronic dynamics within a wide array of basic and applied research projects.

Being able to take advantage of the full potential offered by current and emerging atomic scale photoelectron imaging techniques relies on theoretical and numerical modeling. This is true for comparatively simple atoms in the gas phase, and for complex nanostructured targets additional theoretical challenges arise [6,20]. While for atomic photoionization by visible and near UV light, the size of the target is small compared to the wavelength of the incident light pulse, this is no longer true for x-ray ionization, leading to the well-known breakdown of the dipole approximation [51,52]. Furthermore, for nanoparticles [22–28], (nanostructured) surfaces [36,53–55], and layered structures [31,35,36,42], not only the comparability of the wavelength and structure size requires careful quantum-mechanical modeling beyond the dipole approximation, but also the target’s spatially inhomogeneous dielectric response to the incident light pulse [54,55]. Most numerical models for streaked and interferometric photoemission from atoms are based on the so-called “strong-field approximation” (SFA) [6]. The SFA builds on the assumption that photoemitted electrons are solely exposed to *spatially homogeneous* external fields. It discards all other interactions photoreleased electrons may be subject to (e.g., with the residual parent ion) and cannot accommodate spatially inhomogeneous final-state interactions.

While the SFA was shown to deteriorate for lower photoelectron energies [56], it completely loses its applicability for complex targets as screening and plasmonic effects expose photoelectrons to *inhomogeneous* net electromagnetic fields [6,38,54,55]. The convenient use of analytically known

so-called ‘‘Volkov wave functions’’ for the photoelectron’s motion in homogeneous electromagnetic fields [57] is no longer acceptable since dielectric response effects entail screening length and induced plasmonic fields at the nm length scale [22,24–28,36,38]. Thus, the numerical modeling of photoemission from complex targets with morphologies or plasmonic response lengths at the nm scale by intense short wavelength pulses [made increasingly available at new (X)FEL light sources [49,50]], necessitates photoemission models beyond the SFA.

To this effect, we previously employed heuristically generalized Volkov states to model photoemission from bare and adsorbate-covered metal surfaces [35,36,54,55] and plasmonic nanoparticles [22,26,28]. While this allowed us to numerically model streaked [42,54,55,58] and interferometric photoemission spectra from surfaces [35,36], in fair to good agreement with experimental data, and to reconstruct plasmonic fields near gold nanospheres [28], a systematic mathematical solution of the time-dependent Schrödinger (TDSE) for a single active electron exposed to inhomogeneous external fields remains to be explored. We here discuss a semiclassical model for obtaining such solutions. While being approximate, our complex-phase Wentzel-Kramer-Brillouin (WKB) type approach lends itself to systematic iterative refinement. Our proposed method, termed ACCTIVE (action calculation by classical trajectory integration in varying electromagnetic fields), employs complex classical trajectories to solve the TDSE in the presence of spatially inhomogeneous electromagnetic pulses that are represented by time-dependent inhomogeneous scalar and vector potentials. Our approach is inspired by the semiclassical complex-trajectory method for solving the TDSE with time-independent scalar interactions of Boiron and Lombardi [59] and its adaptation to time-dependent scalar interactions by Goldfarb, Schiff, and Tannor [60].

Following the mathematical formulation of ACCTIVE in Sec. II, we validate this method by discussing five examples in Sec. III. We first compare ACCTIVE calculations with *ab initio* numerical solutions by scrutinizing electronic states in a (i) homogeneous laser field, (ii) Coulomb field, and (iii) combination of laser and Coulomb fields. Next, we apply ACCTIVE to streaked photoemission from (iv) hydrogen atoms and (v) plasmonic nanoparticles. In the application to Au nanospheres, we examine final states for the simultaneous interaction of the photoelectron with the spatially inhomogeneous plasmonically enhanced field induced by the streaking infrared (IR) laser pulse and demonstrate the improved reconstruction of the induced nanoplasmonic IR field from streaked photoemission spectra. Section IV contains our summary. In four appendices we prove the gauge invariance of the ACCTIVE method (Appendix A) and add details of our calculations within ACCTIVE of Volkov wave functions (Appendix B) and Coulomb wave functions (Appendix C), and additional comments on streaked photoemission from Au nanospheres (Appendix D).

II. THEORY

We seek approximate solutions of the TDSE for a particle of (effective) mass m and charge q in an inhomogeneous

time-dependent electromagnetic field given by the scalar and vector potentials $\phi(\mathbf{r}, t)$ and $\mathbf{A}(\mathbf{r}, t)$ and any additional scalar potential $V(\mathbf{r}, t)$:

$$i\hbar \frac{\partial}{\partial t} \Psi(\mathbf{r}, t) = \left\{ \frac{1}{2m} [i\hbar \nabla + q\mathbf{A}(\mathbf{r}, t)]^2 + \varphi(\mathbf{r}, t) \right\} \Psi(\mathbf{r}, t), \quad (1)$$

where $\varphi(\mathbf{r}, t) = q\phi(\mathbf{r}, t) + V(\mathbf{r}, t)$. Representing the wave function in eikonal form, $\Psi(\mathbf{r}, t) = e^{iS(\mathbf{r}, t)/\hbar}$, Eq. (1) can be rewritten in terms of the complex-valued quantum-mechanical action $S(\mathbf{r}, t)$ as

$$\begin{aligned} \frac{\partial}{\partial t} S(\mathbf{r}, t) + \frac{1}{2m} [\nabla S(\mathbf{r}, t) - q\mathbf{A}(\mathbf{r}, t)]^2 + \varphi(\mathbf{r}, t) \\ = \frac{i\hbar}{2m} \nabla \cdot [\nabla S(\mathbf{r}, t) - q\mathbf{A}(\mathbf{r}, t)]. \end{aligned} \quad (2)$$

Expanding the action in powers of \hbar [59,60],

$$S(\mathbf{r}, t) = \sum_{n=0}^{\infty} \hbar^n S_n(\mathbf{r}, t), \quad (3)$$

substituting Eq. (3) into Eq. (2), and comparing terms of equal order results in the set of coupled partial differential equations

$$\frac{\partial}{\partial t} S_0(\mathbf{r}, t) + \frac{[\nabla S_0(\mathbf{r}, t) - q\mathbf{A}(\mathbf{r}, t)]^2}{2m} + \varphi(\mathbf{r}, t) = 0, \quad (4a)$$

$$\begin{aligned} \frac{\partial}{\partial t} S_1(\mathbf{r}, t) + \left[\frac{\nabla S_0(\mathbf{r}, t) - q\mathbf{A}(\mathbf{r}, t)}{m} \right] \cdot \nabla S_1(\mathbf{r}, t) \\ = \frac{i}{2} \nabla \cdot \left[\frac{\nabla S_0(\mathbf{r}, t) - q\mathbf{A}(\mathbf{r}, t)}{m} \right], \end{aligned} \quad (4b)$$

$$\begin{aligned} \frac{\partial}{\partial t} S_n(\mathbf{r}, t) + \left[\frac{\nabla S_0(\mathbf{r}, t) - q\mathbf{A}(\mathbf{r}, t)}{m} \right] \cdot \nabla S_n(\mathbf{r}, t) \\ = -\frac{1}{2m} \sum_{j=1}^{n-1} \nabla S_j(\mathbf{r}, t) \cdot \nabla S_{n-j}(\mathbf{r}, t) \\ + \frac{i}{2m} \nabla^2 S_{n-1}(\mathbf{r}, t) \quad (n \geq 2), \end{aligned} \quad (4c)$$

where the lowest-order contribution $S_0(\mathbf{r}, t)$ is the classical action of a charged particle moving in the electromagnetic field

$$\begin{aligned} \mathbf{E}(\mathbf{r}, t) &= -\nabla\phi(\mathbf{r}, t)/q - \partial\mathbf{A}(\mathbf{r}, t)/\partial t, \\ \mathbf{B}(\mathbf{r}, t) &= \nabla \times \mathbf{A}(\mathbf{r}, t). \end{aligned} \quad (5)$$

With regard to the ongoing discussion about the gauge (in)variance of approximate solutions of the TDSE for intense-external field interactions with matter (see, e.g., [52,61,62] and references therein), we point out that Eqs. (4) are form invariant under gauge transformations

$$\begin{aligned} \mathbf{A} &\mapsto \mathbf{A}' = \mathbf{A} + \nabla f(\mathbf{r}, t), \\ \varphi &\mapsto \varphi' = \varphi - q \frac{\partial}{\partial t} f(\mathbf{r}, t), \end{aligned} \quad (6)$$

defined in terms of arbitrary differentiable functions $f(\mathbf{r}, t)$ that leave the external fields $\mathbf{E}(\mathbf{r}, t)$ and $\mathbf{B}(\mathbf{r}, t)$ unchanged. This invariance requires the classical action to transform

according to

$$\begin{aligned} S_0(\mathbf{r}, t) &\mapsto S'_0(\mathbf{r}, t) = S_0(\mathbf{r}, t) + qf(\mathbf{r}, t), \\ S_n(\mathbf{r}, t) &\mapsto S'_n(\mathbf{r}, t) = S_n(\mathbf{r}, t) \quad (n \geq 1), \end{aligned} \quad (7)$$

in agreement with the known unitary local gauge transformation of the wave function $\Psi(\mathbf{r}, t)$ according to $\Psi(\mathbf{r}, t) \mapsto \Psi'(\mathbf{r}, t) = e^{iqf(\mathbf{r}, t)/\hbar} \Psi(\mathbf{r}, t)$ [51,62]. Here, the complex phase $qf(\mathbf{r}, t)/\hbar$ appears only in $S_0(\mathbf{r}, t)$. For further comments see Appendix A.

Solving the classical Hamilton-Jacobi equation (HJE) (4a) leads to Newton's second law

$$\frac{d}{dt} \mathbf{v}(\mathbf{r}, t) = \frac{q}{m} [\mathbf{E}(\mathbf{r}, t) + \mathbf{v}(\mathbf{r}, t) \times \mathbf{B}(\mathbf{r}, t)], \quad (8)$$

where the classical velocity field $\mathbf{v}(\mathbf{r}, t)$ and kinetic momentum

$$\mathbf{p}(\mathbf{r}, t) \equiv m\mathbf{v}(\mathbf{r}, t) \equiv \nabla S_0(\mathbf{r}, t) - q\mathbf{A}(\mathbf{r}, t) \quad (9)$$

are given in terms of the gauge-invariant canonical momentum $\nabla S_0(\mathbf{r}, t)$ [63] (see Appendix A). The combination of the HJE (4a) and Eq. (9) provides the Lagrangian $L[\mathbf{r}, \mathbf{v}(\mathbf{r}, t), t]$ as a total time differential of $S_0(\mathbf{r}, t)$:

$$\begin{aligned} \frac{d}{dt} S_0(\mathbf{r}, t) &= L[\mathbf{r}, \mathbf{v}(\mathbf{r}, t), t] \\ &= \frac{1}{2} m \mathbf{v}^2(\mathbf{r}, t) + q\mathbf{v}(\mathbf{r}, t) \cdot \mathbf{A}(\mathbf{r}, t) - \varphi(\mathbf{r}, t). \end{aligned} \quad (10)$$

Similarly, by substituting Eq. (9) into Eqs. (4b) and (12), we find the total time derivatives of the first-order contribution to $S(\mathbf{r}, t)$,

$$\frac{d}{dt} S_1(\mathbf{r}, t) = \frac{i}{2} \nabla \cdot \mathbf{v}(\mathbf{r}, t), \quad (11)$$

and of all higher-order terms

$$\begin{aligned} \frac{d}{dt} S_n(\mathbf{r}, t) &= -\frac{1}{2m} \sum_{j=1}^{n-1} \nabla S_j(\mathbf{r}, t) \cdot \nabla S_{n-j}(\mathbf{r}, t) \\ &\quad + \frac{i}{2m} \nabla^2 S_{n-1}(\mathbf{r}, t) \quad (n \geq 2). \end{aligned} \quad (12)$$

Approximate solutions to $S(\mathbf{r}, t)$ can be obtained by iteration of Eq. (12), after integrating the total time derivatives in Eqs. (10), (11), and (12) along classical trajectories $\tilde{\mathbf{r}}(t)$ that are defined by

$$\frac{d}{dt} \tilde{\mathbf{r}}(t) \equiv \mathbf{v}[\tilde{\mathbf{r}}(t), t] \quad (13)$$

with respect to a reference time (integration constant) t_r . The wave function at t_r , $\Psi_r(\mathbf{r}) = \Psi(\mathbf{r}, t_r)$, provides initial ($t_r \ll 0$) or asymptotic ($t_r \gg 0$) conditions in terms of the action

$$S(\mathbf{r}, t_r) = -i\hbar \ln[\Psi_r(\mathbf{r})] \quad (14)$$

and the velocity field

$$\begin{aligned} \mathbf{v}(\mathbf{r}, t_r) &= -\frac{1}{m} \nabla S_0(\mathbf{r}, t_r) - \frac{q}{m} \mathbf{A}(\mathbf{r}, t_r) \\ &\approx -\frac{1}{m} \nabla S(\mathbf{r}, t_r) - \frac{q}{m} \mathbf{A}(\mathbf{r}, t_r) \\ &= -\frac{i\hbar \nabla \Psi_r(\mathbf{r})}{m \Psi_r(\mathbf{r})} - \frac{q}{m} \mathbf{A}(\mathbf{r}, t_r). \end{aligned} \quad (15)$$

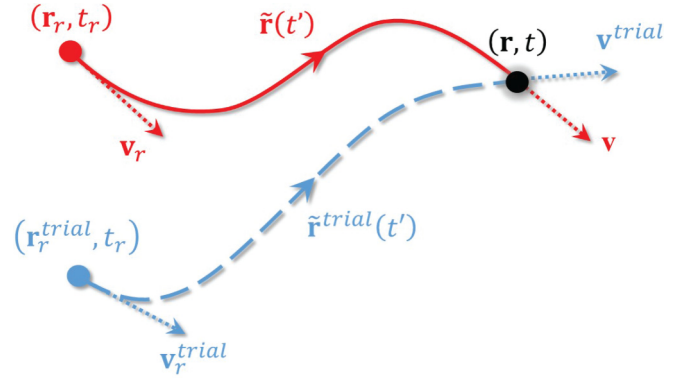


FIG. 1. Illustration of the shooting method used for determining classical trajectories. For any given event (\mathbf{r}, t) and a predetermined reference time t_r , trajectories are classically propagated from trial points in phase space $(\mathbf{r}, \mathbf{v}^{\text{trial}})$ at time t along trial trajectories $\tilde{\mathbf{r}}^{\text{trial}}(t')$. The velocity field \mathbf{v} and appropriate trajectory $\tilde{\mathbf{r}}(t')$ are determined by iterating the trial velocity $\mathbf{v}^{\text{trial}}$ in order to find the roots of $f(\mathbf{v}^{\text{trial}})$ in Eq. (18).

The semiclassical solution of Eqs. (10), (11), and (12) requires an appropriate classical trajectory $\tilde{\mathbf{r}}(t')$, for any given “current” event (\mathbf{r}, t) that connects the “current” coordinate and velocity,

$$\mathbf{r} = \tilde{\mathbf{r}}(t), \quad \mathbf{v} = \left. \frac{d\tilde{\mathbf{r}}(t')}{dt'} \right|_t, \quad (16)$$

to the proper coordinate and velocity at t_r ,

$$\mathbf{r}_r = \tilde{\mathbf{r}}(t_r), \quad (17a)$$

$$\mathbf{v}_r = \left. \frac{d\tilde{\mathbf{r}}(t')}{dt'} \right|_{t_r} = -\frac{i\hbar \nabla \Psi_r(\mathbf{r}_r)}{m \Psi_r(\mathbf{r}_r)} - \frac{q}{m} \mathbf{A}(\mathbf{r}_r, t_r). \quad (17b)$$

The known quantities in Eqs. (16) and (17) are \mathbf{r} , t , and t_r , while \mathbf{v} , \mathbf{r}_r , and \mathbf{v}_r are to be determined. To numerically calculate the undetermined quantities, we employ a shooting method, starting with a “trial” velocity $\mathbf{v}^{\text{trial}}$ at position \mathbf{r} and time t . Propagating \mathbf{r} to the reference time according to Eq. (8) results in $\mathbf{r}_r^{\text{trial}} = \tilde{\mathbf{r}}^{\text{trial}}(t_r)$ and $\mathbf{v}_r^{\text{trial}} = d\tilde{\mathbf{r}}^{\text{trial}}(t')/dt'|_{t_r}$ (Fig. 1).

The velocity field \mathbf{v} that satisfies Eq. (8) can now be found numerically by determining the roots of the function

$$f(\mathbf{v}^{\text{trial}}) = \left| \mathbf{v}_r^{\text{trial}} + \frac{i\hbar \nabla \Psi_r(\mathbf{r}_r^{\text{trial}})}{m \Psi_r(\mathbf{r}_r^{\text{trial}})} + \frac{q}{m} \mathbf{A}(\mathbf{r}_r^{\text{trial}}, t_r) \right| \quad (18)$$

for an appropriate range of start trial velocities. In our numerical applications, this is accomplished by an efficient multi-dimensional quasi-Newton root-finding algorithm (Broyden's method) [64,65]. Once the correct trajectories $\tilde{\mathbf{r}}(t')$ are determined by finding the roots of Eq. (18), the actions in Eqs. (10), (11), and (12) are integrated along these trajectories and composed, by truncating Eq. (3), into an approximate solution of Eq. (1).

Since each term $S_n(\mathbf{r}, t)$ in Eq. (3) depends only on terms of lower orders, ACCTIVE enables, in principle, the systematic iterative refinement of approximate solutions of Eq. (1) by including successively higher orders n . The iteration is started with $S_0(\mathbf{r}, t)$, which is determined by the velocity field $\mathbf{v}(\mathbf{r}, t)$, and continued by integrating Eqs. (11) and (12).

In the numerical examples discussed in Sec. III below, we find that retaining only the zeroth- and first-order terms $S_0(\mathbf{r}, t)$ and $S_1(\mathbf{r}, t)$ provides sufficiently accurate and physically meaningful solutions at modest numerical expense. Thus, according to Eqs. (10) and (11), we apply

$$\begin{aligned} \Psi(\mathbf{r}, t) &\approx \exp\{iS_0(\mathbf{r}, t)/\hbar + iS_1(\mathbf{r}, t)\} \\ &= e^{iS(\mathbf{r}, t_r)/\hbar} \exp\left\{-\frac{1}{2} \int_{t_r}^t \nabla \cdot \mathbf{v}(\tilde{\mathbf{r}}(t'), t') dt' \right. \\ &\quad \left. + \frac{i}{\hbar} \int_{t_r}^t L[\tilde{\mathbf{r}}(t'), \mathbf{v}(\tilde{\mathbf{r}}(t'), t'), t'] dt'\right\}. \end{aligned} \quad (19)$$

For real classical trajectories and potentials, the integral of $S_0(\mathbf{r}, t)$ is real, representing a local phase factor, while $S_1(\mathbf{r}, t)$ is purely imaginary and defines the wave-function amplitude, as in the standard WKB approach [51]. The quantum-mechanical probability density $\rho(\mathbf{r}, t)$ then satisfies the continuity equation

$$\frac{d\rho(\mathbf{r}, t)}{dt} = \frac{d}{dt} |\Psi(\mathbf{r}, t)|^2 = -\rho(\mathbf{r}, t) \nabla \cdot \mathbf{v}(\mathbf{r}, t) \quad (20)$$

for the classical probability flux $\rho(\mathbf{r}, t) \mathbf{v}(\mathbf{r}, t)$ [66].

III. EXAMPLES

We validate the ACCTIVE method by discussing five applications to electron wave functions in Coulomb and laser fields.

A. Volkov wave function

For the simple example of an electron in a time-dependent, spatially homogeneous laser field, the potentials in Eq. (1) and reference wave function are (in the Coulomb electromagnetic gauge [51])

$$\mathbf{A}(\mathbf{r}, t) = \mathbf{A}(t), \quad \varphi(\mathbf{r}, t) = 0, \quad \Psi_r(\mathbf{r}) = e^{i\mathbf{p}\cdot\mathbf{r}/\hbar}, \quad (21)$$

and the first-order wave function in Eq. (19) reproduces the well-known analytical Volkov solution [57]

$$\Psi^V(\mathbf{r}, t) = \exp\left\{\frac{i\mathbf{p}\cdot\mathbf{r}}{\hbar} - \frac{i}{2m\hbar} \int_{t_r}^t [\mathbf{p} - q\mathbf{A}(t')]^2 dt'\right\}. \quad (22)$$

For details of the derivation of Eq. (22) within ACCTIVE, see Appendix B.

B. Coulomb wave function

As a second simple example and limiting case, we consider an unbound electron in the Coulomb field of a proton. In this case, the potentials in Eq. (1) are

$$\mathbf{A}(\mathbf{r}, t) = 0, \quad \varphi(\mathbf{r}, t) = -k_e \frac{e^2}{r}, \quad (23)$$

where e is the elementary charge and k_e the electrostatic constant. Assuming outgoing-wave boundary conditions, we define the reference wave function at a sufficiently large reference time t_r as the “outgoing” Coulomb wave

$$\Psi_r(\mathbf{r}, t_r) \xrightarrow{t_r \rightarrow \infty, z \rightarrow +\infty} e^{i(kz - \frac{\hbar k^2}{2m} t_r)}. \quad (24)$$

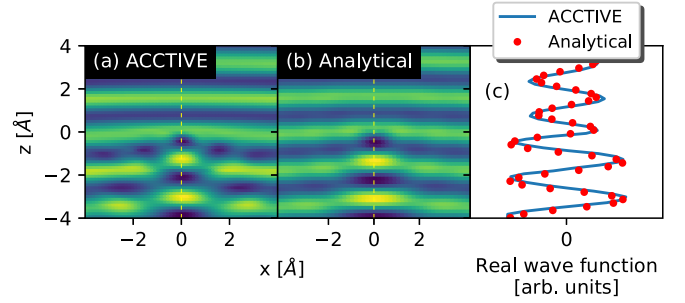


FIG. 2. Real part of an unbound Coulomb wave function, subject to the boundary condition given by an outgoing wave propagating along the z axis. (a) Numerically calculated semiclassical first-order ACCTIVE wave function. (b) Analytical Coulomb wave function in the $y = 0$ plane. (c) Real part of the wave functions in (a) and (b) along the z axis for $x = y = 0$.

Here, $\mathbf{r} = (x, y, z)$ and $p = \hbar k > 0$ is the final electron momentum. In this case, the TDSE is solved exactly by the well-known Coulomb wave function

$$\Psi_k^C(\mathbf{r}, t) = \frac{e^{\frac{\pi}{2k}} \Gamma(1 - i/k)}{(2\pi)^{3/2}} {}_1F_1(i/k, 1, ikr - ikz) e^{i(kz - \frac{\hbar k^2}{2m} t)} \quad (25)$$

in terms of the confluent hypergeometric function ${}_1F_1$. Note that for finite distances from the z axis (i.e., for finite coordinates x and y), the asymptotic form of the Coulomb continuum wave function for $z \rightarrow +\infty$ is just a plane wave (without a logarithmic phase term) [51, 67].

Applying ACCTIVE to the outgoing-wave Coulomb problem, t_r must be chosen sufficiently long after t , so that each classical trajectory $\tilde{\mathbf{r}}(t')$ propagates far enough toward the $z \rightarrow +\infty$ asymptotic limit for the reference velocity to become

$$\mathbf{v}_r \xrightarrow{t_r \rightarrow \infty, z \rightarrow +\infty} \hat{\mathbf{z}} p/m, \quad (26)$$

in compliance with Eq. (17b). In this and for the following numerical example, we use as reference velocity the initial trial velocity for points of the spatial numerical grid that are sufficiently far away from the Coulomb singularity at the origin. The correct “current” velocities $\mathbf{v}(\mathbf{r}, t)$ at the most distant coordinates are subsequently used as trial velocities at the nearest-neighbor spatial grid points. This scheme is continued until classical trajectories for the entire spatiotemporal numerical grid are calculated. Further details of the numerical calculation of Coulomb wave functions within ACCTIVE are given in Appendix C.

Figure 2 shows the very good agreement between the numerically calculated first-order ACCTIVE wave function (19) and the analytical Coulomb wave function (25) for a final electron kinetic energy of $p^2/2m = 50$ eV. The color (grayscale) represents the real part of the wave function in the x - z plane. Figures 2(a) and 2(b) show the same scattering pattern. Good quantitative agreement of the first-order ACCTIVE wave function and the analytical Coulomb wave function is demonstrated in Fig. 2(c).

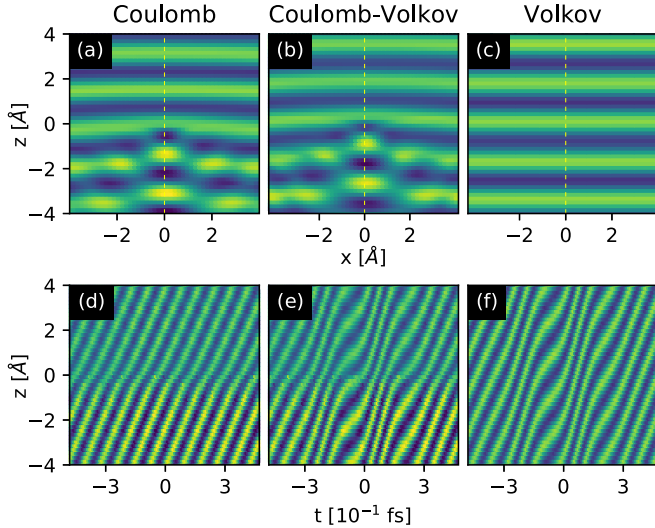


FIG. 3. Real parts of (a), (d) Coulomb, (b), (e) ACCTIVE-calculated Coulomb-Volkov, and (c), (f) Volkov wave functions in the $y = 0$ plane. (a)–(c) Snapshots at time $t = 0$, when the laser-pulse center is at $z = 0$. (d)–(f) Time evolution along the z axis.

C. Coulomb-Volkov wave function

A more challenging third example is given by the motion of an electron under the combined influence of a point charge (proton), located at the coordinate origin, and a spatially homogeneous laser pulse, subject to the boundary condition (24). In this case, the potentials in Eq. (1) are (in Coulomb gauge [51])

$$\mathbf{A}(\mathbf{r}, t) = \mathbf{A}(t), \quad \varphi(\mathbf{r}, t) = -k_e \frac{e^2}{r}. \quad (27)$$

Considering a laser pulse of finite duration, t_r must be chosen such that the laser electric field vanishes at t_r . This combination of the two previous examples in Secs. III A and III B constitutes the Coulomb-Volkov problem, for which merely approximate solutions [68–71], but no analytical wave function, are known. We assume a laser pulse with 15 eV central photon energy, a cosine-square temporal intensity envelope with a pulse length of 0.5 fs full width at half intensity maximum (FWHM), and 3×10^{15} W/cm² peak intensity. At time $t = 0$, the temporal pulse profile is centered at $z = 0$. We enforce the outgoing-wave boundary condition (24) for an asymptotic photoelectron kinetic energy of $p^2/2m = 50$ eV. This energy is reached at a sufficiently large distance of the outgoing electron from the proton and long after the pulse has vanished.

In Fig. 3 we compare the ACCTIVE-calculated Coulomb-Volkov wave function with Coulomb and Volkov wave functions for identical outgoing-wave boundary condition and 50-eV asymptotic photoelectron kinetic energy. The Coulomb and Volkov wave functions are given for a positive elementary charge and the same laser parameters as the Coulomb-Volkov wave, respectively. The color (grayscale) represents the real part of the wave functions. We determined all numerical parameters (numerical grid size, spacing, and propagation time step) to ensure convergence of the wave functions.

Figures 3(a), 3(b), and 3(c) display snapshots at time $t = 0$ of the Coulomb, ACCTIVE-calculated Coulomb-Volkov, and Volkov wave functions, respectively. The Coulomb-Volkov wave function shows a similar (inverse) Coulomb scattering pattern for the incident wave ($z < 0$) as the Coulomb wave. Its outgoing part ($z > 0$) closely matches the phase of the Volkov wave. On the other hand, the time-dependent evolution of the Coulomb-Volkov wave function in the $y = 0$ plane in Fig. 3(e) shows laser-induced wavefront distortions, similar to the Volkov wave in Fig. 3(f). The time evolution of the ACCTIVE-calculated Coulomb-Volkov wave function reveals the acceleration of the incoming and deceleration of the outgoing wave near the proton at $z = 0$ of the pure Coulomb wave in Fig. 3(d). An animated version of this wave-function comparison can be found in the Supplemental Material [72].

D. Streaked photoemission from hydrogen atoms

As a fourth example, we employ ACCTIVE final-state wave functions to calculate IR-streaked XUV photoelectron spectra from ground-state hydrogen atoms [6]. We assume the ionizing XUV and streaking IR pulse as linearly polarized along the z axis. The relative time delay between the centers of the two pulses τ is assumed positive in case the IR precedes XUV pulse. The electric field $E_X(t)$ of the XUV pulse is characterized by a Gaussian temporal profile, 55 eV central photon energy, and a pulse length of 200 as (FWHM). The IR pulse has a cosine-squared temporal profile, 720 nm central wavelength, pulse duration of 2 fs FWHM, and 10^{11} W/cm² peak intensity.

We model streaked photoemission from the ground state of hydrogen $|\Psi_i\rangle$ based on the quantum-mechanical transition amplitude [6,28,51,55]

$$T(\mathbf{k}_f, \tau) \sim \int dt \langle \Psi_{\mathbf{k}_f, \tau}^{C-V} | z E_X(t) | \Psi_i \rangle, \quad (28)$$

where the IR-pulse-dressed final state of the photoelectron $|\Psi_{\mathbf{k}_f, \tau}^{C-V}\rangle$ is a Coulomb-Volkov wave function [56] that we evaluate numerically using the ACCTIVE method. In a comparison calculation, we replace the Coulomb-Volkov state by the Volkov state $|\Psi_{\mathbf{k}_f, \tau}^V\rangle$ and assume otherwise identical physical conditions. As mentioned in the Introduction, the use of Volkov states [57] in photoionization calculations is referred to as SFA [6] and amounts to neglecting the interaction of the released photoelectron with the residual ion (proton in the present case). We scrutinize streaked photoemission spectra obtained with ACCTIVE-calculated Coulomb-Volkov final states and in SFA against *ab initio* benchmark calculations. In these exact numerical calculations we directly solve the three-dimensional TDSE using the SCID-TDSE time-propagation code [73].

Numerical results are shown in Fig. 4. The streaked photoemission spectra obtained with ACCTIVE-calculated Coulomb-Volkov final states [Fig. 4(a)], in SFA [Fig. 4(b)], and by direct numerical solution of the TDSE [Fig. 4(c)] show

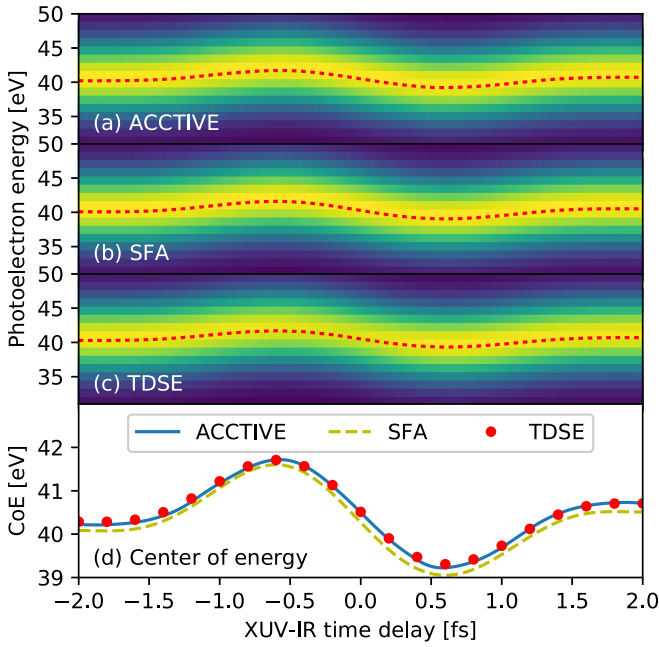


FIG. 4. IR-streaked XUV photoelectron spectra, (a) based on ACCTIVE-calculated Coulomb-Volkov final states, (b) in SFA, and (c) obtained by direct numerical solution of the TDSE. Red dotted lines in (a)–(c) indicate the respective centers of energy (CoE). The spectral yields in (a)–(c) are normalized separately, to their respective maxima. (d) Comparison of the delay-dependent CoE for the spectra in (a)–(c).

very similar “streaking traces,” i.e., oscillations of the asymptotic photoelectron energy with delay τ . For a quantitative comparison, we plot in Fig. 4(d) the centers of energy (CoEs) of the spectra in Figs. 4(a)–4(c). While the three calculations result in identical photoemission phase shifts (streaking time delays) relative to the streaking IR field, within the resolution of the graph, the ACCTIVE-calculated spectra agree with the exact TDSE calculation, while the SFA calculation predicts noticeably smaller CoEs due to the neglect of the Coulomb potential in the final photoelectron state [22].

E. Streaked photoemission from metal nanospheres

As a final, fifth, example, we apply the ACCTIVE method to model photoelectron states in *spatially inhomogeneous*, plasmonically enhanced IR electromagnetic fields. For this purpose, we investigate streaked photoemission [22,25–27] and the reconstruction of plasmonic near fields [28] for gold nanospheres with a radius of $R = 50$ nm. We represent the electronic structure of the nanosphere in terms of eigenstates of a square well with a potential depth of $V_0 = -13.1$ eV and obtain the photoelectron yield by incoherently adding the transition amplitudes (28) over all occupied initial conduction-band states [6,55,58]. For the calculation of the transition amplitude (28), we closely follow Ref. [26], with the important difference of employing numerically calculated semiclassical ACCTIVE final photoelectron wave functions, while in Ref. [26] the SFA approximation is used, applying heuristically generalized Volkov final states and thus neglecting direct photoelectron interactions with the residual nanoparticle.

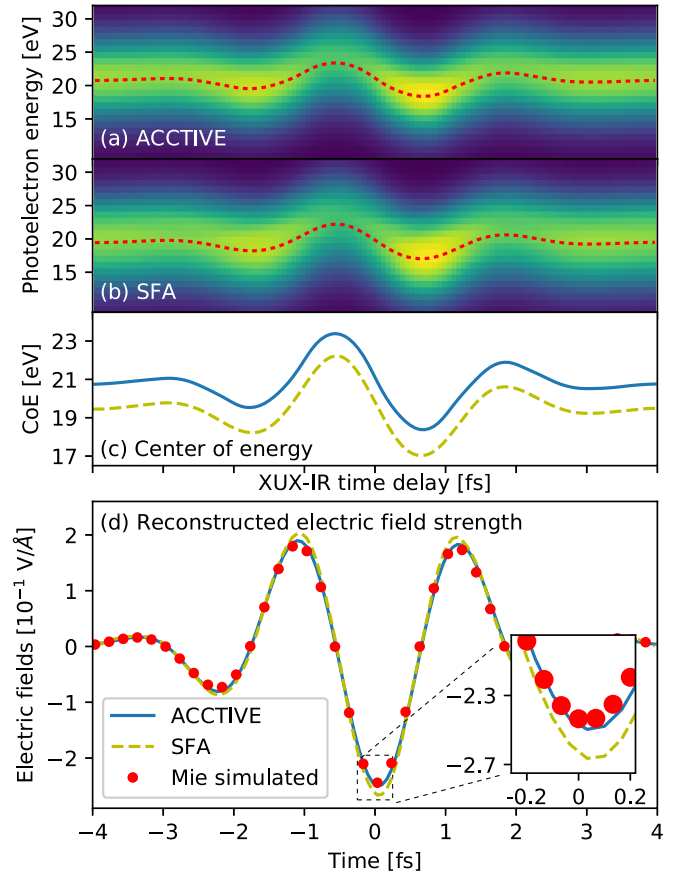


FIG. 5. Simulated IR-streaked XUV photoelectron spectra for photoemission along the XUV-pulse polarization direction (a) using ACCTIVE final states and (b) in SFA. (c) Corresponding delay-dependent centers of energy. (d) Comparison of the corresponding reconstructed plasmonic electric near fields at the point $(x, y, z) = (0, 0, R)$ on the nanoparticle surface with the Mie-theory-calculated electric field.

For the ACCTIVE calculation we thus solve the TDSE (1) with the potentials

$$\mathbf{A}(\mathbf{r}, t) = \int_t^\infty \mathbf{E}_{\text{tot}}(\mathbf{r}, t') dt', \quad (29a)$$

$$\varphi(\mathbf{r}, t) = \begin{cases} V_0, & r < R \\ 0, & r \geq R \end{cases} \quad (29b)$$

and the boundary condition (24). Here, the asymptotic wave function in Eq. (24) also serves as reference wave function for the classical trajectory computation. The net time-dependent inhomogeneous field $\mathbf{E}_{\text{tot}}(\mathbf{r}, t)$ is given by the superposition of the homogeneous IR field of the incident streaking pulse and the inhomogeneous plasmonic field produced by the nanoparticle in response to the incident IR pulse [27,28]. For the streaking calculation, we assume an XUV pulse with 30 eV central photon energy and Gaussian temporal profile with a width of 200 as (FWHM). We further suppose a delayed Gaussian IR pulse with 720 nm central wavelength, 2.47 fs (FWHM) pulse length, and 5×10^{10} W/cm² peak intensity.

Figure 5 shows simulated streaked photoelectron spectra obtained with ACCTIVE-calculated and Volkov final states

for electron emission along the XUV-pulse polarization direction. In this direction, the effect of the induced plasmonic field on the photoelectron is strongest [28]. The corresponding spectra in Figs. 5(a) and 5(b) show very similar temporal oscillations of the photoelectron yield and CoE as a function of both asymptotic photoelectron energy and XUV-IR pulse delay τ . As for streaked photoemission from hydrogen atoms discussed in Sec. III D above, we find that the SFA shifts the CoE to lower kinetic energies [Fig. 5(b), cf. Fig. 4(d)]. Here, the SFA results in an approximately 1.5 eV lower CoE than the ACCTIVE calculation. This energy shift is due to the fact that the SFA, by neglecting the potential well of the nanosphere in the final photoelectron state, leads to an unphysical enhancement of the photoemission cross section at lower photoelectron kinetic energies, thereby increasing the weight of low-energy yields in the CoE average [22]. Additional comments on the comparison of streaked photoelectron spectra within either ACCTIVE or based on Volkov wave functions can be found in Appendix D.

From streaked photoemission spectra the plasmonic near field at the nanoparticle surface can be reconstructed as detailed in Refs. [27,28]. Figure 5(d) shows the reconstructed net electric field \mathbf{E}_{tot} along the XUV-pulse polarization direction, i.e., at the surface and on the positive z axis, of the nanosphere. The reconstruction of net plasmonically enhanced near fields from the simulated spectra in Figs. 5(a) and 5(b) was performed according to the scheme proposed in Ref. [28]. The obtained reconstructed fields are compared in Fig. 5(d) with the net electric IR near field obtained within Mie theory [74] and used as input in the streaking calculations. As is seen in Fig. 5(d), the ACCTIVE method improves the near-field reconstruction in comparison with the SFA calculation. The least-square deviation between the reconstructed and Mie-theory calculated fields, assembled over the entire IR pulse length, amounts to 1.62% using the ACCTIVE wave function and 3.05% using the SFA. A comparative animation of reconstructed and analytical electric fields at the surface of Au nanospheres can be found in the Supplemental Material [72]. The ACCTIVE method thus extends the applicability of the plasmonic near-field reconstruction scheme in Ref. [28] to lower XUV photon energies.

IV. SUMMARY

In summary, we propose a semiclassical method, ACC-TIVE, to solve the TDSE for one active electron exposed to any spatially inhomogeneous time-dependent external force field. We validate this method by comparing ACCTIVE-calculated electronic wave functions with known Coulomb and Volkov wave functions for the electronic dynamics in Coulomb and intense laser fields, respectively, and by scrutinizing ACCTIVE-calculated Coulomb-Volkov final photoelectron wave functions (i) against *ab initio* numerical solutions of the TDSE and (ii) in streaked photoemission from hydrogen atoms and plasmonic metal nanospheres.

For streaked photoemission from hydrogen atoms, we demonstrate excellent agreement of our ACCTIVE calculation with a benchmark *ab initio* TDSE calculation, while a comparative calculation using the SFA systematically deviates from the exact TDSE solution. For streaked photoemission

from Au nanospheres we find that ACCTIVE final-state wave functions improve the reconstruction of plasmonic near fields over SFA calculations (based on Volkov final states) at comparatively low photoelectron energies.

ACKNOWLEDGMENTS

This work was supported in part by the Chemical Sciences, Geosciences, and Biosciences Division, Office of Basic Energy Sciences, Office of Science, U.S. Department of Energy under Award No. DEFG02-86ER13491 (attosecond interferometry), NSF Grant No. PHY 1802085 (theory of photoemission from surfaces), and the Air Force Office of Scientific Research Award No. FA9550-17-1-0369 (recollision physics at the nanoscale).

APPENDIX A: GAUGE INVARIANCE OF THE ACCTIVE METHOD

While Eq. (1) is known to be form invariant under the gauge transformations given by Eqs. (6) [51], we here verify the invariance of Eqs. (4) under the transformations (6) and (7).

We first show that the velocity field (9) is gauge invariant. This is easily demonstrated by the following steps:

$$\begin{aligned} \mathbf{p}'(\mathbf{r}, t) &\equiv m\mathbf{v}'(\mathbf{r}, t) \\ &\equiv \nabla S'_0(\mathbf{r}, t) - q\mathbf{A}'(\mathbf{r}, t) \\ &= \nabla[S_0(\mathbf{r}, t) + qf(\mathbf{r}, t)] - q[\mathbf{A}(\mathbf{r}, t) + \nabla f(\mathbf{r}, t)] \\ &= \nabla S_0(\mathbf{r}, t) - q\mathbf{A}(\mathbf{r}, t) \\ &\equiv \mathbf{p}(\mathbf{r}, t) \equiv m\mathbf{v}(\mathbf{r}, t). \end{aligned} \quad (\text{A1})$$

Next, the sequence of identities

$$\begin{aligned} 0 &= \frac{\partial}{\partial t} S_0(\mathbf{r}, t) + \frac{[\nabla S_0(\mathbf{r}, t) - q\mathbf{A}(\mathbf{r}, t)]^2}{2m} + \varphi(\mathbf{r}, t) \\ &= \frac{\partial}{\partial t} [S'_0(\mathbf{r}, t) - qf(\mathbf{r}, t)] + \frac{[\nabla S'_0(\mathbf{r}, t) - q\mathbf{A}'(\mathbf{r}, t)]^2}{2m} \\ &\quad + \left[\varphi'(\mathbf{r}, t) + q\frac{\partial}{\partial t} f(\mathbf{r}, t) \right] \\ &= \frac{\partial}{\partial t} S'_0(\mathbf{r}, t) + \frac{[\nabla S'_0(\mathbf{r}, t) - q\mathbf{A}'(\mathbf{r}, t)]^2}{2m} + \varphi'(\mathbf{r}, t) \end{aligned} \quad (\text{A2})$$

proves the gauge invariance of Eq. (4a). The invariance of the higher-order terms in Eqs. (4b) and (4c) is easily recognized by replacing $S_n(\mathbf{r}, t)$ with $S'_n(\mathbf{r}, t)$ for $n \geq 1$ and $[S_0(\mathbf{r}, t) - q\mathbf{A}(\mathbf{r}, t)]$ with $[S'_0(\mathbf{r}, t) - q\mathbf{A}'(\mathbf{r}, t)]$.

APPENDIX B: DERIVATION OF EQ. (22)

We here derive the Volkov wave function (22) using ACC-TIVE. Starting from the potentials and initial wave function in Eq. (21), the velocity field along the classical trajectory $\tilde{\mathbf{r}}(t)$ is

$$\mathbf{v}(\mathbf{r}, t) = \frac{\mathbf{p}}{m} + \frac{q}{m} \int_{t_0}^t \mathbf{E}(t') dt' = \frac{\mathbf{p} - q\mathbf{A}(t)}{m}. \quad (\text{B1})$$

Therefore,

$$\tilde{\mathbf{r}}(t) = \mathbf{r}_0 + \int_{t_0}^t \left[\frac{\mathbf{p} - q\mathbf{A}(t')}{m} \right] dt', \quad (\text{B2})$$

$$\nabla \cdot \mathbf{v}(\mathbf{r}, t) = 0, \quad (\text{B3})$$

and Eq. (19), applied to the example in Sec. III A, becomes

$$\begin{aligned} \Psi(\mathbf{r}, t) &= \exp \left\{ \frac{i\mathbf{p} \cdot \mathbf{r}_0}{\hbar} + \frac{i}{\hbar} \int_{t_0}^t \left[\frac{m}{2} \left(\frac{\mathbf{p} - q\mathbf{A}(t')}{m} \right)^2 + q \left(\frac{\mathbf{p} - q\mathbf{A}(t')}{m} \right) \cdot \mathbf{A}(t') \right] dt' \right\} \\ &= \exp \left\{ \frac{i\mathbf{p}}{\hbar} \cdot \left[\mathbf{r} - \int_{t_0}^t \left(\frac{\mathbf{p} - q\mathbf{A}(t')}{m} \right) dt' \right] + \frac{i}{\hbar} \int_{t_0}^t \left[\frac{m}{2} \left(\frac{\mathbf{p} - q\mathbf{A}(t')}{m} \right)^2 + q \left(\frac{\mathbf{p} - q\mathbf{A}(t')}{m} \right) \cdot \mathbf{A}(t') \right] dt' \right\} \\ &= \exp \left\{ \frac{i\mathbf{p} \cdot \mathbf{r}}{\hbar} + \frac{i}{\hbar} \int_{t_0}^t \left[\frac{m}{2} \left(\frac{\mathbf{p} - q\mathbf{A}(t')}{m} \right)^2 - m \left(\frac{\mathbf{p} - q\mathbf{A}(t')}{m} \right)^2 \right] dt' \right\} \\ &= \exp \left\{ \frac{i\mathbf{p} \cdot \mathbf{r}}{\hbar} - \frac{i}{2m\hbar} \int_{t_0}^t [\mathbf{p} - q\mathbf{A}(t')]^2 dt' \right\}, \end{aligned} \quad (\text{B4})$$

which is the Volkov wave function (22).

APPENDIX C: NUMERICAL CALCULATION OF COULOMB WAVE FUNCTIONS USING ACCTIVE

The ACCTIVE method links a quantum-mechanical problem of obtaining wave functions $\Psi(\mathbf{r}, t)$ to a classical problem of determining velocity fields $\mathbf{v}(\mathbf{r}, t)$. However, in some cases, e.g., for Coulomb wave functions, such velocity fields are not uniquely defined (Fig. 6). This can result in interference patterns in the obtained wave functions, as pointed out by Goldfarb *et al.* [60].

For each event (\mathbf{r}, t) , two possible classical trajectories can be found to satisfy the same boundary condition of an outgoing plane wave in Eq. (24), as shown in Fig. 6. Goldfarb *et al.* [60] take this interference into account by approximating the wave function as the superposition of contributions from

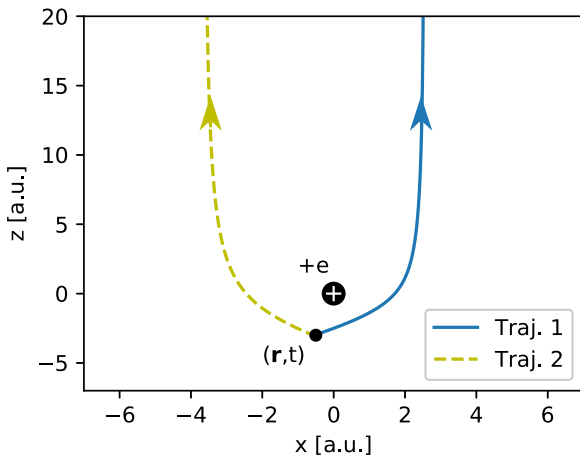


FIG. 6. Two possible classical trajectories passing through (\mathbf{r}, t) satisfying the same outgoing plane-wave boundary condition.

different trajectories

$$\Psi(\mathbf{r}, t) \approx \sum_l \exp \left[\frac{i}{\hbar} S^l(\tilde{\mathbf{r}}(t), t) \right], \quad (\text{C1})$$

where each action $S^l(\mathbf{r}, t)$ is associated with a trajectory $\tilde{\mathbf{r}}^l(t)$. In this work, we follow a different and simpler approach.

The TDSE is a linear partial differential equation. Its solution can be expressed as the superposition of a set of linearly independent basis functions $\Psi^l(\mathbf{r}, t)$,

$$\Psi(\mathbf{r}, t) = \sum_l C^l \Psi^l(\mathbf{r}, t) = \sum_l C^l \exp \left[\frac{i}{\hbar} S^l(\mathbf{r}, t) \right], \quad (\text{C2})$$

where each $S^l(\mathbf{r}, t)$ is uniquely determined by a velocity field $\mathbf{v}^l(\mathbf{r}, t)$ and the coefficients C^l are obtained from the initial condition

$$\Psi_0(\mathbf{r}) = \sum_l C^l \Psi^l(\mathbf{r}, t_0). \quad (\text{C3})$$

Since two possible trajectories can be obtained for each given event (\mathbf{r}, t) , we can find two velocity fields $\mathbf{v}^+(\mathbf{r}, t)$ and $\mathbf{v}^-(\mathbf{r}, t)$, which are defined by

$$\mathbf{v}^+(\mathbf{r}, t) \xrightarrow{z \rightarrow +\infty, x > 0} \hat{\mathbf{z}}p/m, \quad (\text{C4a})$$

$$\mathbf{v}^-(\mathbf{r}, t) \xrightarrow{z \rightarrow +\infty, x < 0} \hat{\mathbf{z}}p/m, \quad (\text{C4b})$$

as illustrated in Figs. 7(a) and 7(b), respectively. Figures 7(c) and 7(d) show the calculated first-order ACCTIVE wave functions, $\Psi^+(\mathbf{r}, t)$ and $\Psi^-(\mathbf{r}, t)$, associated with these two velocity fields at $t = 0$. Numerical calculation shows that

$$\Psi^+(\mathbf{r}, t) \xrightarrow{z \rightarrow +\infty} \begin{cases} e^{ikz}, & x > 0 \\ 0, & x < 0 \end{cases} \quad (\text{C5a})$$

$$\Psi^-(\mathbf{r}, t) \xrightarrow{z \rightarrow +\infty} \begin{cases} e^{ikz}, & x < 0 \\ 0, & x > 0. \end{cases} \quad (\text{C5b})$$

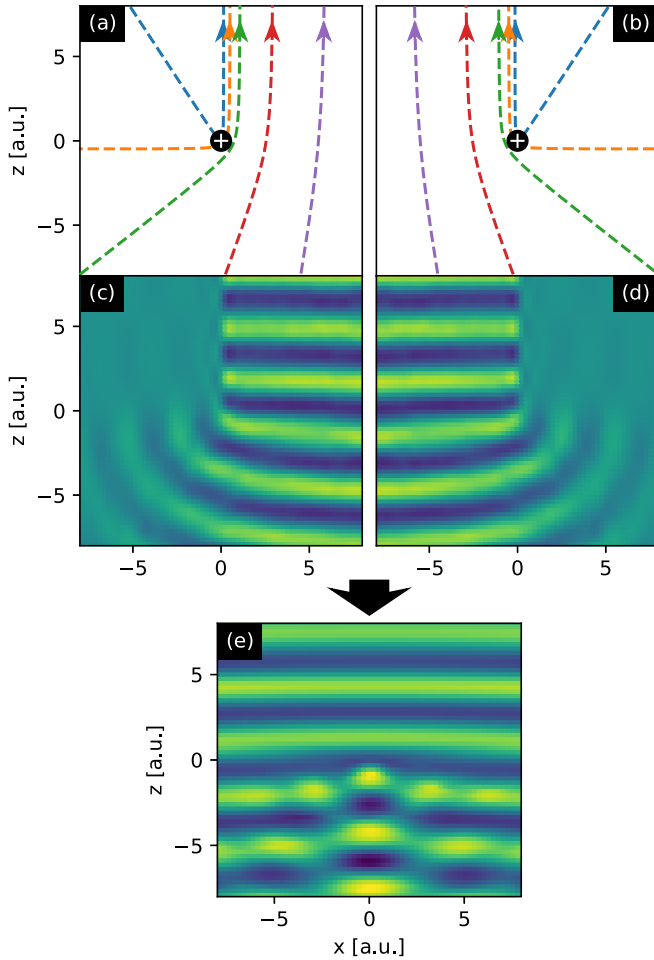


FIG. 7. Two possible velocity fields (a) $\mathbf{v}^+(\mathbf{r}, t)$ and (b) $\mathbf{v}^-(\mathbf{r}, t)$. (c) $\Psi^+(\mathbf{r}, t)$ and (d) $\Psi^-(\mathbf{r}, t)$ are the real parts of the corresponding first-order ACCTIVE wave functions at $y = 0$ plane, respectively, and (e) $\Psi(\mathbf{r}, t)$ is the linear combination of these two wave functions.

Therefore, at t_0 , $\Psi_0(\mathbf{r}) = \Psi(\mathbf{r}, 0)$ can be written as the linear combination of $\Psi^+(\mathbf{r}, t_0)$ and $\Psi^-(\mathbf{r}, t_0)$ and satisfies the boundary condition (C4):

$$\Psi_0(\mathbf{r}) = \Psi^+(\mathbf{r}, t_0) + \Psi^-(\mathbf{r}, t_0). \quad (\text{C6})$$

The wave function at any given time t is then obtained with the same coefficients,

$$\Psi(\mathbf{r}, t) = \Psi^+(\mathbf{r}, t) + \Psi^-(\mathbf{r}, t), \quad (\text{C7})$$

and is shown in Fig. 7(e).

APPENDIX D: COMMENTS ON STREAKED PHOTOEMISSION FROM Au NANOSPHERES

Figure 5 in the main text shows the comparison of simulated streaked photoelectron spectra using either ACCTIVE wave functions as final states or Volkov wave function in SFA. ACCTIVE wave functions are more accurate at low

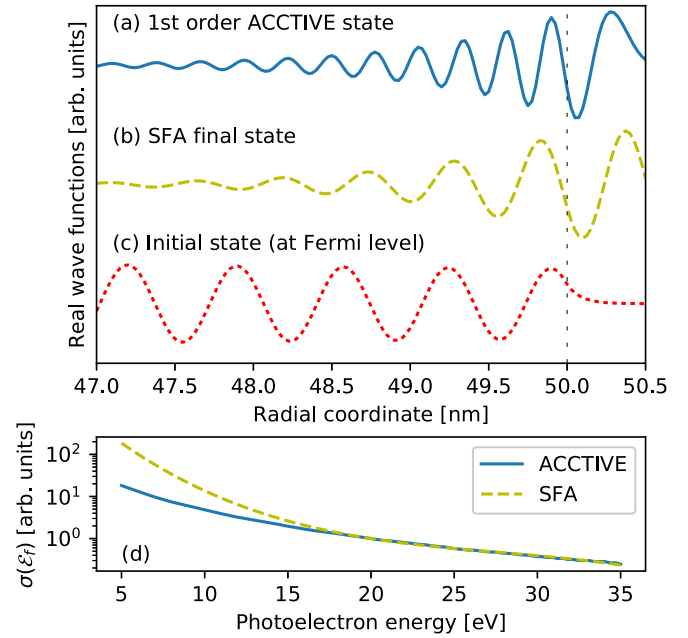


FIG. 8. Real parts of photoelectron final-state wave functions near the surface of Au nanospheres along the XUV polarization direction: (a) first-order ACCTIVE wave function and (b) SFA modeled wave function in Ref. [28], for the electron detection along the XUV polarization direction and asymptotic photoelectron energy $\mathcal{E}_f = 5$ eV. (c) Initial-state wave function, modeled as bound state in a spherical square-well potential, at the Fermi level. The vertical dashed line indicates the nanosphere surface. (d) Simulated XUV photoemission cross sections.

photoelectron energy, but entail higher CoEs than Volkov wave functions [Fig. 5(c)]. In comparison with Fig. 4(d), this might appear as counterintuitive. An explanation is given below.

Figure 8(a) shows the real part of the first-order ACCTIVE wave function near the Au nanosphere surface, and Fig. 8(b) the corresponding Volkov wave function in SFA [28]. Both are calculated for photoelectron detection along the XUV polarization direction and outgoing photoelectron energy $\mathcal{E}_f = 5$ eV. Inside the nanosphere, the Volkov final-state wave function neglects the spherical well potential. It therefore has a longer wavelength than the ACCTIVE wave function and more strongly overlaps with the initial-state wave function shown in Fig. 8(c). Thus, the cross section, calculated following Ref. [51], is larger in SFA than if based on ACCTIVE final states.

This effect becomes less significant at larger photoelectron kinetic energies, where both ACCTIVE and SFA wave functions have shorter wavelengths and overlap less with initial-state wave function. Figure 8(d) shows that the energy-dependent photoemission cross sections calculated with ACCTIVE and Volkov final states converge at large photoelectron energies, while at small energies the SFA leads to larger cross sections. The net effect of this cross-section difference is to put more weight on photoelectron yields at lower energy and thus to shift streaking traces and CoEs in SFA photoemission spectra to lower energies as compared to ACCTIVE-calculated spectra.

- [1] S. Hüfner, *Photoelectron Spectroscopy. Principles and Applications* (Springer, Berlin, 2003).
- [2] M. Hentschel, R. Kienberger, C. Spielmann, G. A. Reider, N. Milosevic, T. Brabec, P. Corkum, U. Heinzmann, M. Drescher, and F. Krausz, *Nature (London)* **414**, 509 (2001).
- [3] Z. Chang, *Phys. Rev. A* **70**, 043802 (2004).
- [4] G. Sansone, E. Benedetti, F. Calegari, C. Vozzi, L. Avaldi, R. Flammini, L. Poletto, P. Villoresi, C. Altucci, R. Velotta, S. Stagira, S. De Silvestri, and M. Nisoli, *Science* **314**, 443 (2006).
- [5] F. Krausz and M. Ivanov, *Rev. Mod. Phys.* **81**, 163 (2009).
- [6] U. Thumm, Q. Liao, E. M. Bothschafter, F. Süßmann, M. F. Kling, and R. Kienberger, in *The Oxford Handbook of Innovation*, edited by D. Andrew (Wiley, New York, 2015), Chap. 13.
- [7] P. M. Paul, E. S. Toma, P. Breger, G. Mullot, F. Augé, P. Balcou, H. G. Muller, and P. Agostini, *Science* **292**, 1689 (2001).
- [8] K. Klünder, J. M. Dahlström, M. Gisselbrecht, T. Fordell, M. Swoboda, D. Guénot, P. Johnsson, J. Caillat, J. Mauritsson, A. Maquet, R. Taïeb, and A. L'Huillier, *Phys. Rev. Lett.* **106**, 143002 (2011).
- [9] R. Locher, L. Castiglioni, M. Lucchini, M. Greif, L. Gallmann, J. Osterwalder, M. Hengsberger, and U. Keller, *Optica* **2**, 405 (2015).
- [10] M. Drescher, M. Hentschel, R. Kienberger, M. Uiberacker, V. Yakovlev, A. Scrinzi, T. Westerwalbesloh, U. Kleineberg, U. Heinzmann, and F. Krausz, *Nature (London)* **419**, 803 (2002).
- [11] R. Kienberger, E. Goulielmakis, M. Uiberacker, A. Baltuska, V. Yakovlev, F. Bammer, A. Scrinzi, T. Westerwalbesloh, U. Kleineberg, U. Heinzmann, M. Drescher, and F. Krausz, *Nature (London)* **427**, 817 (2004).
- [12] P. Johnsson, J. Mauritsson, T. Remetter, A. L'Huillier, and K. J. Schafer, *Phys. Rev. Lett.* **99**, 233001 (2007).
- [13] H. Wang, M. Chini, S. Chen, C.-H. Zhang, F. He, Y. Cheng, Y. Wu, U. Thumm, and Z. Chang, *Phys. Rev. Lett.* **105**, 143002 (2010).
- [14] M. Schultze, M. Fieß, N. Karpowicz, J. Gagnon, M. Korbman, M. Hofstetter, S. Neppl, A. L. Cavalieri, Y. Komninos, T. Mercouris, C. A. Nicolaides, R. Pazourek, S. Nagele, J. Feist, J. Burgdörfer, A. M. Azzeer, R. Ernstorfer, R. Kienberger, U. Kleineberg, E. Goulielmakis *et al.*, *Science* **328**, 1658 (2010).
- [15] C. Ott, A. Kaldun, P. Raith, K. Meyer, M. Laux, J. Evers, C. H. Keitel, C. H. Greene, and T. Pfeifer, *Science* **340**, 716 (2013).
- [16] B. Bernhardt, A. R. Beck, X. Li, E. R. Warrick, M. J. Bell, D. J. Haxton, C. W. McCurdy, D. M. Neumark, and S. R. Leone, *Phys. Rev. A* **89**, 023408 (2014).
- [17] H. Niikura, F. Légaré, R. Hasbani, M. Y. Ivanov, D. M. Villeneuve, and P. B. Corkum, *Nature (London)* **421**, 826 (2003).
- [18] M. F. Kling, C. Siedschlag, A. J. Verhoef, J. I. Khan, M. Schultze, T. Uphues, Y. Ni, M. Uiberacker, M. Drescher, F. Krausz, and M. J. J. Vrakking, *Science* **312**, 246 (2006).
- [19] A. Staudte, D. Pavičić, S. Chelkowski, D. Zeidler, M. Meckel, H. Niikura, M. Schöffler, S. Schössler, B. Ulrich, P. P. Rajeev, T. Weber, T. Jahnke, D. M. Villeneuve, A. D. Bandrauk, C. L. Cocke, P. B. Corkum, and R. Dörner, *Phys. Rev. Lett.* **98**, 073003 (2007).
- [20] S. R. Leone, C. W. McCurdy, J. Burgdörfer, L. S. Cederbaum, Z. Chang, N. Dudovich, J. Feist, C. H. Greene, M. Ivanov, R. Kienberger, U. Keller, M. F. Kling, Z.-H. Loh, T. Pfeifer, A. N. Pfeiffer, R. Santra, K. Schafer, A. Stolow, U. Thumm, and M. J. J. Vrakking, *Nat. Photonics* **8**, 162 (2014).
- [21] B. Förg, J. Schötz, F. Süßmann, M. Förster, M. Krüger, B. Ahn, W. A. Okell, K. Wintersperger, S. Zherebtsov, A. Guggenmos, V. Pervak, A. Kessel, S. A. Trushin, A. M. Azzeer, M. I. Stockman, D. Kim, F. Krausz, P. Hommelhoff, and M. F. Kling, *Nat. Commun.* **7**, 11717 (2016).
- [22] J. Li, E. Saydanzad, and U. Thumm, *Phys. Rev. A* **94**, 051401(R) (2016).
- [23] L. Seiffert, Q. Liu, S. Zherebtsov, A. Trabattoni, P. Rupp, M. C. Castrovilli, M. Galli, F. Süßmann, K. Wintersperger, J. Stierle, G. Sansone, L. Poletto, F. Frassetto, I. Halfpap, V. Mondes, C. Graf, E. Rühl, F. Krausz, M. Nisoli, T. Fennel *et al.*, *Nat. Phys.* **13**, 766 (2017).
- [24] J. Schötz, B. Förg, M. Förster, W. A. Okell, M. I. Stockman, F. Krausz, P. Hommelhoff, and M. F. Kling, *IEEE J. Sel. Top. Quantum Electron.* **23**, 77 (2017).
- [25] E. Saydanzad, J. Li, and U. Thumm, *Phys. Rev. A* **95**, 053406 (2017).
- [26] J. Li, E. Saydanzad, and U. Thumm, *Phys. Rev. A* **95**, 043423 (2017).
- [27] E. Saydanzad, J. Li, and U. Thumm, *Phys. Rev. A* **98**, 063422 (2018).
- [28] J. Li, E. Saydanzad, and U. Thumm, *Phys. Rev. Lett.* **120**, 223903 (2018).
- [29] M. Lucchini, A. Ludwig, L. Kasmi, L. Gallmann, and U. Keller, *Opt. Express* **23**, 8867 (2015).
- [30] C. Chen, Z. Tao, A. Carr, P. Matyba, T. Szilvási, S. Emmerich, M. Piecuch, M. Keller, D. Zusin, S. Eich, M. Rollinger, W. You, S. Mathias, U. Thumm, M. Mavrikakis, M. Aeschlimann, P. M. Oppeneer, H. Kapteyn, and M. Murnane, *Proc. Natl. Acad. Sci. USA* **114**, E5300 (2017).
- [31] S. Neppl, R. Ernstorfer, A. L. Cavalieri, C. Lemell, G. Wachter, E. Magerl, E. M. Bothschafter, M. Jobst, M. Hofstetter, U. Kleineberg, J. V. Barth, D. Menzel, J. Burgdörfer, P. Feulner, F. Krausz, and R. Kienberger, *Nature (London)* **517**, 342 (2015).
- [32] Z. Tao, C. Chen, T. Szilvási, M. Keller, M. Mavrikakis, H. Kapteyn, and M. Murnane, *Science* **353**, 62 (2016).
- [33] F. Siek, S. Neb, P. Bartz, M. Hensen, C. Strüber, S. Fiechter, M. Torrent-Sucarrat, V. M. Silkin, E. E. Krasovskii, N. M. Kabachnik, S. Fritzsche, R. D. Muiño, P. M. Echenique, A. K. Kazansky, N. Müller, W. Pfeiffer, and U. Heinzmann, *Science* **357**, 1274 (2017).
- [34] L. Kasmi, M. Lucchini, L. Castiglioni, P. Kliuiev, J. Osterwalder, M. Hengsberger, L. Gallmann, P. Krüger, and U. Keller, *Optica* **4**, 1492 (2017).
- [35] M. J. Ambrosio and U. Thumm, *Phys. Rev. A* **97**, 043431 (2018).
- [36] M. J. Ambrosio and U. Thumm, *Phys. Rev. A* **100**, 043412 (2019).
- [37] M. Ossiander, J. Riemensberger, S. Neppl, M. Mittermair, M. Schäffer, A. Duensing, M. S. Wagner, R. Heider, M. Wurzer, M. Gerl, M. Schnitzenbaumer, J. V. Barth, F. Libisch, C. Lemell, J. Burgdörfer, P. Feulner, and R. Kienberger, *Nature (London)* **561**, 374 (2018).
- [38] C.-H. Zhang and U. Thumm, *Phys. Rev. A* **84**, 063403 (2011).
- [39] S. H. Chew, F. Süßmann, C. Späth, A. Wirth, J. Schmidt, S. Zherebtsov, A. Guggenmos, A. Oelsner, N. Weber, J. Kapaldo, A. Gliserin, M. I. Stockman, M. F. Kling, and U. Kleineberg, *Appl. Phys. Lett.* **100**, 051904 (2012).
- [40] M. Lupetti, J. Hengster, T. Uphues, and A. Scrinzi, *Phys. Rev. Lett.* **113**, 113903 (2014).

- [41] C. Lemke, C. Schneider, T. Leißner, D. Bayer, J. W. Radke, A. Fischer, P. Melchior, A. B. Evlyukhin, B. N. Chichkov, C. Reinhardt, M. Bauer, and M. Aeschlimann, *Nano Lett.* **13**, 1053 (2013).
- [42] Q. Liao and U. Thumm, *Phys. Rev. A* **92**, 031401(R) (2015).
- [43] A. E. Schlather, A. Manjavacas, A. Lauchner, V. S. Marangoni, C. J. DeSantis, P. Nordlander, and N. J. Halas, *J. Phys. Chem. Lett.* **8**, 2060 (2017).
- [44] M. T. Sheldon, J. van de Groep, A. M. Brown, A. Polman, and H. A. Atwater, *Science* **346**, 828 (2014).
- [45] E. Le Ru and P. Etchegoin, *Principles of Surface-Enhanced Raman Spectroscopy: And Related Plasmonic Effects* (Elsevier, Oxford, 2008).
- [46] A. V. Kabashin, P. Evans, S. Pastkovsky, W. Hendren, G. A. Wurtz, R. Atkinson, R. Pollard, V. A. Podolskiy, and A. V. Zayats, *Nat. Mater.* **8**, 867 (2009).
- [47] C. Ayala-Orozco, C. Urban, M. W. Knight, A. S. Urban, O. Neumann, S. W. Bishnoi, S. Mukherjee, A. M. Goodman, H. Charron, T. Mitchell, M. Shea, R. Roy, S. Nanda, R. Schiff, N. J. Halas, and A. Joshi, *ACS Nano* **8**, 6372 (2014).
- [48] F. Krausz and M. I. Stockman, *Nat. Photonics* **8**, 205 (2014).
- [49] Free-Electron Lasers. A collection of recent articles on FEL generation and characterization and their application in fundamental studies of light-matter interaction. *Nat. Photonics Collection* (January 23, 2019).
- [50] J. Duris, S. Li, T. Driver, E. G. Champenois, J. P. MacArthur, A. A. Lutman, Z. Zhang, P. Rosenberger, J. W. Aldrich, R. Coffee, G. Coslovich, F.-J. Decker, J. M. Glowina, G. Hartmann, W. Helml, A. Kamalov, J. Knurr, J. Krzywinski, M.-F. Lin, J. P. Marangos *et al.*, *Nat. Photonics* **14**, 30 (2020).
- [51] E. Merzbacher, *Quantum Mechanics*, 3rd ed. (Wiley, New York, 1998), pp. 73ff, 115, 315ff, 491, 496.
- [52] R. Anzaki, Y. Shinohara, T. Sato, and K. L. Ishikawa, *Phys. Rev. A* **98**, 063410 (2018).
- [53] B. Obreshkov and U. Thumm, *Phys. Rev. A* **74**, 012901 (2006).
- [54] Q. Liao and U. Thumm, *Phys. Rev. Lett.* **112**, 023602 (2014).
- [55] Q. Liao and U. Thumm, *Phys. Rev. A* **89**, 033849 (2014).
- [56] C.-H. Zhang and U. Thumm, *Phys. Rev. A* **82**, 043405 (2010).
- [57] D. M. Wolkow, *Z. Phys.* **94**, 250 (1935).
- [58] C.-H. Zhang and U. Thumm, *Phys. Rev. Lett.* **102**, 123601 (2009).
- [59] M. Boiron and M. Lombardi, *J. Chem. Phys.* **108**, 3431 (1998).
- [60] Y. Goldfarb, J. Schiff, and D. J. Tannor, *J. Chem. Phys.* **128**, 164114 (2008).
- [61] W. Becker and Milosevic, *Laser Phys.* **19**, 1621 (2009).
- [62] A. D. Bandrauk, F. Fillion-Gourdeau, and E. Lorin, *J. Phys. B: At., Mol. Opt. Phys.* **46**, 153001 (2013).
- [63] H. Goldstein, C. Poole, and J. Safko, *Classical Mechanics*, 3rd ed. (Addison-Wesley, Boston, 2001), pp. 22–23,342,433.
- [64] C. G. Broyden, *Math. Comput.* **19**, 577 (1965).
- [65] K. E. Atkinson, *An Introduction to Numerical Analysis* (Wiley, Canada, 2008).
- [66] G. K. Batchelor, *An Introduction to Fluid Dynamics* (Cambridge University Press, Cambridge, 1967), p. 74.
- [67] L. D. Landau and E. M. Lifshitz, *Quantum Mechanics: Non-relativistic Theory*, 3rd ed. (Elsevier, Amsterdam, 1977), p. 570.
- [68] L. Rosenberg and F. Zhou, *Phys. Rev. A* **47**, 2146 (1993).
- [69] H. R. Reiss and V. P. Krainov, *Phys. Rev. A* **50**, R910 (1994).
- [70] P. A. Macri, J. E. Miraglia, and M. S. Gravielle, *J. Opt. Soc. Am. B* **20**, 1801 (2003).
- [71] J. Dubois, S. A. Berman, C. Chandre, and T. Uzer, *Phys. Rev. A* **99**, 053405 (2019).
- [72] See Supplemental Material at <http://link.aps.org/supplemental/10.1103/PhysRevA.101.013411> for animations of the (a) wave-function comparison and (b) Mie-theory-calculated and reconstructed electric near-field distributions for Au nanospheres.
- [73] S. Patchkovskii and H. Muller, *Comput. Phys. Commun.* **199**, 153 (2016).
- [74] G. Mie, *Ann. Phys. (Berlin, Ger.)* **330**, 377 (1908).